


# UNCERTAINTY QUANTIFICATION FOR FISHER-KOLMOGOROV EQUATION ON GRAPHS WITH APPLICATION TO PATIENT-SPECIFIC ALZHEIMER'S DISEASE \*

MATTIA CORTI<sup>1,\*\*</sup> , FRANCESCA BONIZZONI<sup>1</sup>,  
PAOLA F. ANTONIETTI<sup>1</sup> AND ALFIO M. QUARTERONI<sup>1,2</sup>

**Abstract.** The Fisher-Kolmogorov equation is a diffusion-reaction PDE that models the accumulation of prionic proteins, which are responsible for many different neurological disorders. The most important and studied misfolded protein in literature is the Amyloid- $\beta$ , responsible for the onset of Alzheimer's disease. Moving from medical images we construct a reduced-order model based on a graph brain connectome. The reaction coefficient of the proteins which can hardly be measured is modeled as a stochastic random field, taking into account all the many different underlying physical processes. Its probability distribution is inferred by means of the Monte Carlo Markov Chain method applied to clinical data. The resulting model is patient-specific and can be employed for predicting the disease's future development. Forward uncertainty quantification techniques (Monte Carlo and sparse grid stochastic collocation) are applied with the aim of quantifying the impact of the variability of the reaction coefficient on the progression of protein accumulation within the next 20 years.

**Mathematics Subject Classification.** 65N22, 65N75, 65N30.

Received May 5, 2023. Accepted November 17, 2023.

## 1. INTRODUCTION

Neurodegenerative disorders are neurological diseases that yield progressive damage to the neuronal tissue, compromising the communication between cells and then the entire cell structure. Clinical evidence suggests that a mechanism of spreading toxic misfolded prionic proteins stands at the base of neurodegenerative disorders [34]. One of the pathologies in this group is Alzheimer's disease (AD), the most common form of dementia nowadays [28]. In AD, the pathological onset is connected to the accumulation of two proteins, namely the Amyloid- $\beta$  and the tau protein. Their accumulation causes destruction of the synapses that mediate memory and cognition, due to the inability of living neurons to maintain functional axons and dendrites, or to their death [3].

From a clinical point of view, the control of the disease progression is based on cognition exams and on monitoring the value of some critical biomarkers. Amyloid- $\beta$  is the earliest hallmark of AD, for this reason,

---

*Keywords and phrases.* Fisher-Kolmogorov equation, Alzheimer disease, uncertainty quantification, brain connectome, graphs.

\* *Dedicated to the memory of Assyr Abdulle.*

<sup>1</sup> MOX-Dipartimento di Matematica, Politecnico di Milano, Piazza Leonardo da Vinci 32, Milan 20133, Italy.

<sup>2</sup> Institute of Mathematics, École Polytechnique Fédérale de Lausanne, Station 8, Av. Piccard, Lausanne 1015, Switzerland.

\*\*Corresponding author: [mattia.corti@polimi.it](mailto:mattia.corti@polimi.it)

positron emission tomography (PET) is used to evaluate the concentration of the misfolded proteins. However, being invasive and costly [33], PET scanners are often used only for diagnosis and not to monitor the progression of the disease [14].

In this context, the numerical simulation of the misfolded protein concentrations can describe the chemical nature of this type of disease. Several mathematical models for prion dynamics have been proposed in the past few years, based on partial differential equations (PDEs). Oligomer coagulation and fragmentation, which are the chemical processes to which Amyloid- $\beta$  undergoes, are typically described by means of the Smoluchowski equation [10]. Although this model is able to describe in a detailed way the reality of chemical interactions, solving it on three-dimensional meshes of the brain is difficult, due to the prohibitive computational complexity. For this reason, suitable simplified methods have been proposed, based on graphs that represent the principal connections between different brain regions, namely the connectograms. These networks can be derived starting from Diffusion Weighted Images (DWI) and then used as a geometrically reduced order model to compute a numerical solution of the PDEs [9, 12], upon including some patient-specific information inside the graph structure itself.

The same approach is applied in this work: starting from DWI images we derive a brain connectome describing our patient's brain that we use as a discrete space domain for the Fisher-Kolmogorov (FK) equation [9, 35]. The latter can be derived as a simplified version of the complete Smoluchowski model, indeed it reduces to a single nonlinear PDE. For this type of equation simulations of neurodegeneration on a complete brain geometry are mostly based on finite element discretizations [24, 35]. Recently, in [5, 6] the authors proposed numerical methods based on discontinuous Galerkin methods for the approximation of FK equation.

Concerning the simulation of the FK model on graphs, diffusion directions, and magnitude are derived from medical imaging. However, no information about the parameter describing the protein reaction can be obtained from clinical exams. Indeed, due to the simplified form of the equation, the reaction parameter encodes many different physical processes at the same time: production, misfolding, aggregation and clearance [9]. Because of that, some works describe the parameter as a random variable [26]. Indeed, in this work, our approach for the calibration of the parameter makes use of the Amyloid- $\beta$  concentrations derived from two subsequent PET medical images to estimate the probability distribution by means of an inverse uncertainty quantification (UQ) algorithm.

Bayesian inverse UQ algorithms in the context of neurodegenerative disorders have been used in [26], to describe the diffusion and reaction of tau proteins, using the FK equation. In [27], the application of the Bayesian framework is extended to a coupling between the tau protein accumulation and the induced atrophy. In this work, we employ the Markov Chain Monte Carlo (MCMC) method [16, 22] to calibrate the reaction parameter of the FK equation modelling the spreading of Amyloid- $\beta$  protein. As a result, we obtain a patient-specific model describing the disease development.

With the aim of predicting the disease development and assessing the impact of the reaction coefficient variability on the random protein concentration, we apply forward UQ methods. In particular, we introduce the quantity of interest (QoI) being the spatial average of the protein concentration at a set of time instances ( $t = 5, 10, 15, 20$  years), and we estimate its expectation and variance by means of the Monte Carlo (MC) [13] as well as the sparse grid stochastic collocation (SC) method [1, 20]. To the best of our knowledge, this is the first time that the SC method is employed to infer the evolution of neurodegenerative diseases.

The paper is organized as follows. In Section 2, we introduce the FK mathematical model with stochastic reaction parameter and discuss its application to neurodegeneration. Moreover, we introduce the space discretization of the problem on the reconstructed graph. In Section 3 we recall numerical methods for inverse and forward UQ. Numerical results are presented in Section 4: we introduce the numerical discretization and the PET imaging projection (Sect. 4.1), we show the results of the inverse UQ (Sect. 4.2), and we discuss the results of the forward UQ simulations along 20 years (Sect. 4.3). Finally, in Section 5 we draw some conclusions and discuss possible further developments.

## 2. MATHEMATICAL MODEL

In this section, we present the FK equation to describe the reaction and diffusion of Amyloid- $\beta$  proteins. Hence, the problem is dependent on time  $t \in (0, T]$ , with final time  $T > 0$ , and space  $\mathbf{x} \in \Omega \subset \mathbb{R}^d$  ( $d = 2, 3$ ). A typical assumption in the literature is that there exists a constant baseline concentration of healthy state proteins. The problem at hand can be described by only one relative concentration of the misfolded protein  $c$ . Indeed, the variable  $c$  is rescaled in the interval  $[0, 1]$ , where 0 means the absence of misfolded proteins and 1 is the high prevalence of them. For a detailed model derivation, we refer to [35].

We assume that the reaction parameter  $\alpha = \alpha(\mathbf{x}, \mathbf{p})$  representing the local conversion rate of the proteins from healthy to misfolded state depends on the parameter vector  $\mathbf{p} = (p_1, \dots, p_N)$  randomly varying in the hyperrectangle  $\Gamma = \Gamma_1 \times \dots \times \Gamma_N \subseteq \mathbb{R}^N$ . In particular, we assume:

$$\alpha(\mathbf{x}, \mathbf{p}) = \sum_{j=1}^N p_j \chi_{\Omega_j}(\mathbf{x}), \tag{1}$$

where  $(\Omega_j)_{j=1}^N$  is a non-overlapping partition of the domain  $\Omega$  and  $p_j$  denotes the reaction parameter in the region  $\Omega_j$ , for all  $j = 1, \dots, N$ . In this work,  $\Omega_j$ ,  $j = 1, \dots, N$  refers to different regions of the brain and in the considered application  $N = 7$ : frontal lobe, temporal lobe, parietal lobe, insular lobe, limbic lobe, occipital lobe, and subcortical nuclei. As a consequence, the concentration  $c$  depends on the space and time variables as well as on the parameter vector  $\mathbf{p}$ , namely,  $c = c(\mathbf{x}, t, \mathbf{p})$ .

The differential model reads as follows: find  $c: \Omega \times [0, T] \times \Gamma \rightarrow \mathbb{R}$  such that

$$\begin{cases} \frac{\partial c}{\partial t}(\mathbf{x}, t, \mathbf{p}) = \nabla \cdot (\mathbf{D}(\mathbf{x}) \nabla c(\mathbf{x}, t, \mathbf{p})) + \alpha(\mathbf{x}, \mathbf{p}) c(\mathbf{x}, t, \mathbf{p})(1 - c(\mathbf{x}, t, \mathbf{p})) & (\mathbf{x}, t, \mathbf{p}) \in \Omega \times (0, T] \times \Gamma, \\ (\mathbf{D}(\mathbf{x}) \nabla c(\mathbf{x}, t, \mathbf{p})) \cdot \mathbf{n}(\mathbf{x}) = 0 & (\mathbf{x}, t, \mathbf{p}) \in \partial\Omega \times (0, T] \times \Gamma, \\ c(\mathbf{x}, 0, \mathbf{p}) = c_0(\mathbf{x}) & (\mathbf{x}, \mathbf{p}) \in \Omega \times \Gamma. \end{cases} \tag{2}$$

The reaction parameter is assumed to be stochastic since its value is highly patient-specific and depends on the production, misfolding and clearance processes [9, 26]. In particular, the conversion factor models not only the production and aggregation of misfolded protein [3], but also the reduced clearance that is connected with the pathological functioning of the glymphatic system [4]. This variety of processes encoded in the parameter alpha stems from the simplification of the more detailed Smoluchowski model [9] from which the FK equation is derived. The diffusion tensor  $\mathbf{D} = \mathbf{D}(\mathbf{x})$  denotes the spreading of the misfolded protein inside the domain; the latter represents the volume occupied by the whole brain parenchymal tissue. From a biological point of view, most of the diffusion occurs along axonal directions; for this reason, we derive a graph, which connects brain regions from DWI [35]. This graph is typically known as brain connectome [7]. We denote the deterministic initial condition with  $c_0 = c_0(\mathbf{x})$ . Finally, at  $\partial\Omega$ , we assume homogeneous Neumann boundary condition,  $\mathbf{n} = \mathbf{n}(\mathbf{x})$  being the unit normal to  $\partial\Omega$ .

### 2.1. Discrete formulation

Due to the nature of the prionic diffusion, which is mostly aligned along the axonal connections, we discretize equation (2) on the brain connectome graph, following [2, 9]. More in details, we introduce the graph  $\mathcal{G} = (V, E)$  representing a discretization of the domain  $\Omega$ , where  $V = (\mathbf{x}_j)_{j=1}^M$  denotes the set of vertices (nodes) of the graph and  $E$  denotes the set of edges, as it can be observed in Figure 1a. In the construction of the weighted undirected graph, we associate a positive weight  $w_{ij} \geq 0$  to each couple of nodes  $(i, j) \in V \times V$ . In particular,  $w_{ij} = 0$  means that we do not have any connection between the two nodes.

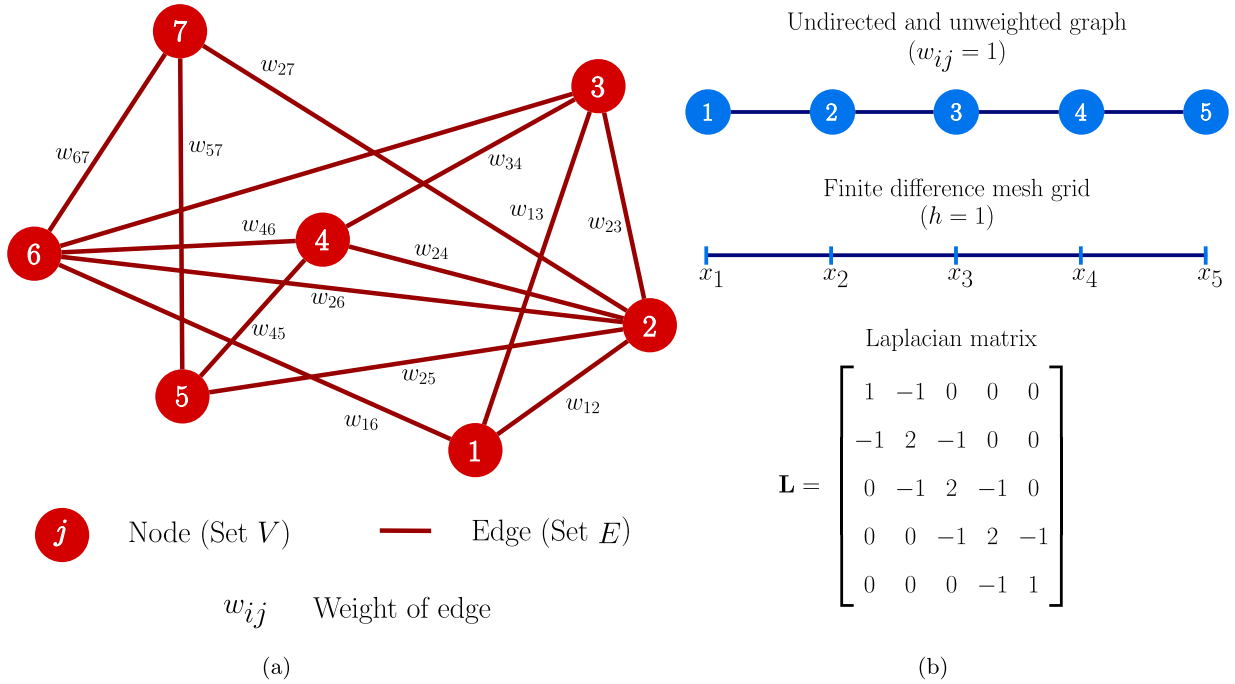


FIGURE 1. Schematic representation of graphs and Laplacina matrix. (a) Monomeric seeding model. (b) Polymeric seeding model.

The graph  $\mathcal{G}$  and its structure allow us to define the Laplacian matrix  $\mathbf{L} = (\mathbf{L}_{ij})_{i,j=1}^M$  [11, 30] as:

$$\mathbf{L}_{ij} = \begin{cases} -w_{ij} & i \neq j, \\ \sum_{j=1}^M w_{ij} & i = j, \end{cases} \quad i, j = 1, \dots, M. \quad (3)$$

This definition applies to weighted and undirected graphs and defines a positive semidefinite symmetric matrix [11]. The definition of  $\mathbf{L}$  depends only on the topological structure of the graph.

The Laplacian matrix in equation (3) can be used to represent a discretization of the continuous Laplacian operator [30]. Indeed, the discretization proposed for the Laplacian of a generic function  $g = g(\mathbf{x})$  in the  $j$ -th node is:

$$\nabla \cdot (\mathbf{D}(\mathbf{x}_j) \nabla g(\mathbf{x}_j)) \simeq \sum_{\substack{i=1 \\ i \neq j}}^M w_{ji} (g(\mathbf{x}_j) - g(\mathbf{x}_i)) = \sum_{i=1}^M \mathbf{L}_{ji} g(\mathbf{x}_i), \quad (4)$$

where the Laplacian matrix  $\mathbf{L}$  represents the weighted diffusion modeled in the continuous limit by the tensor  $\mathbf{D}$ , indeed the weights are connected to the axonal diffusion as explained in Section 4.1. This descends from the discretization of the Laplace operator by means of the finite difference method, on cartesian grids, which can be associated with a lattice, i.e. a regular unweighted graph [11], as shown in Figure 1b. In particular, a graph vertex represents a grid point and its local connectivity determines the finite difference approximation stencil of the grid point. Concerning the boundary condition, following the duality with the finite difference paradigm, the fact that we do not apply any constraint to the grid points. The interpretation of this fact is the application of a homogeneous Neumann boundary condition to the continuous problem [30]. For information

about the application of this discretization to the FK equation, we refer to [9, 12], while concerning the general parabolic semilinear equation, we refer to [18].

Applying the theory of discretization of PDEs on graphs [18] to the model problem (2), we find the following semi-discretized formulation:

$$\begin{cases} \frac{\partial c_j}{\partial t}(t, \mathbf{p}) = - \sum_{i=1}^M \mathbf{L}_{ji} c_i(t, \mathbf{p}) + \alpha(\mathbf{x}_j, \mathbf{p}) c_j(t, \mathbf{p}) (1 - c_j(t, \mathbf{p})) & (t, \mathbf{p}) \in (0, T] \times \Gamma \quad j = 1, \dots, M, \\ c_j(0, \mathbf{p}) = c_{0j} & \mathbf{p} \in \Gamma \quad j = 1, \dots, M. \end{cases} \quad (5)$$

Equation (5) is a system of networked ordinary differential equations (ODEs), where  $c_j(t, \mathbf{p}) \simeq c(\mathbf{x}_j, t, \mathbf{p}) : [0, T] \times \Gamma \rightarrow \mathbb{R}$  is the approximated solution at the  $j$ -th node  $\mathbf{x}_j$  of the graph  $\mathcal{G}$ . The solution evaluated at the set of nodes  $\mathbf{x}_j \in V$  is collected into the vector  $\mathbf{c} = (c_j)_{j=1}^M : [0, T] \times \Gamma \rightarrow \mathbb{R}^M$ . In the same way, the values of the initial condition  $c_0(\mathbf{x})$  at  $V$  are encoded by the vector  $\mathbf{c}_0 = (c_{0j})_{j=1}^M \in \mathbb{R}^M$ , with  $c_{0j} = c_0(\mathbf{x}_j)$  for all  $j = 1, \dots, M$ .

To discretize in time, we apply the Crank-Nicolson scheme, with a second-order extrapolation for a semi-implicit treatment of the nonlinear reactive term. In particular, let  $\{t_\ell\}_{\ell=0}^{N_t}$  be the uniform partition of the time interval  $[0, T]$  into  $N_t$  intervals with length  $\Delta t = \frac{T}{N_t}$ , namely,  $0 = t_0 < t_1 < \dots < t_{N_t} = T$  and  $t_\ell = \frac{\ell T}{N_t}$  for  $\ell = 0, \dots, N_t$ . The fully discrete formulation of problem (2) reads: give the initial conditions  $\mathbf{c}_0$  and  $\mathbf{c}_{-1}$ , find  $\mathbf{c}^{k+1} = \mathbf{c}^{k+1}(\mathbf{p})$ , such that

$$\begin{cases} \frac{\mathbf{c}^{k+1} - \mathbf{c}^k}{\Delta t} = -\frac{1}{2} \mathbf{L} (\mathbf{c}^{k+1} + \mathbf{c}^k) + \boldsymbol{\alpha} \odot \left( \frac{1}{2} \mathbf{c}^{k+1} + \frac{1}{2} \mathbf{c}^k \right) \odot \left( \mathbf{1} - \left( \frac{3}{2} \mathbf{c}^k - \frac{1}{2} \mathbf{c}^{k-1} \right) \right) & k = 0, \dots, N_t - 1, \\ \mathbf{c}^0 = \mathbf{c}_0, \quad \mathbf{c}^{-1} = \mathbf{c}_{-1}, \end{cases} \quad (6)$$

where for each node of the graph  $\mathcal{G}$   $\boldsymbol{\alpha}$  is the vector containing the corresponding value of the reaction parameter  $\alpha$ ,  $\mathbf{1}$  is a vector of ones and the symbol  $\odot$  denotes the (component-by-component) Hadamard product.

### 3. UQ METHODS FOR FK WITH STOCHASTIC REACTION ON GRAPHS

In this section, we describe inverse and forward uncertainty quantification algorithms, which we apply in Section 4. In particular, in Section 3.1, we introduce the MCMC method, and in Section 3.2, we introduce the MC and the SC methods.

#### 3.1. Inverse Uncertainty Quantification

As seen in Section 2, the FK equation (2) depends on the reaction parameter  $\boldsymbol{\alpha}(\mathbf{x}, \mathbf{p})$  defined in equation (1), is a stochastic variable depending on the random vector  $\mathbf{p}$ , encoding several physical processes that cannot be directly estimated. However, due to the patient-specificity of the neurodegeneration, it is difficult to determine a distribution of the components  $(p_1, \dots, p_N)$  that can be used for every patient [26]. For this reason, in this work, we propose to estimate specific distributions of the parameters, starting from the PET medical images and using the MCMC method.

Let us denote with  $\mathcal{Q} \in \mathbb{R}$  the QoI, or output, of the fully-discrete FK formulation (6). It can be seen as a function of the  $N$  uncertain parameters, namely  $\mathcal{Q} : \Gamma \rightarrow \mathbb{R}$ , even though generalizations to the vector-valued case are straightforward. Possible examples are the spatial average of the solution at the final time

$$\mathcal{Q}(\mathbf{p}) = \langle c \rangle(T, \mathbf{p}) = \frac{1}{M} \sum_{i=1}^M c_i(T, \mathbf{p}), \quad (7)$$

(see Sect. 4) or the solution at one specific node  $x_{j^*}$  at the final time ( $\mathcal{Q}(\mathbf{p}) = c_{j^*}(T, \mathbf{p})$ ).

In order to determine the distribution of the parameter vector  $\mathbf{p} = (p_1, \dots, p_N) \in \Gamma$ , we construct a Markov chain, by extracting at every iteration a step from a Gaussian distribution  $\boldsymbol{\delta} \sim \mathcal{N}(\mathbf{0}, \widehat{\Sigma})$  totally independent from the previous one, where we assume that  $\widehat{\Sigma} = \widehat{\sigma}^2 \mathbf{I}$ , with  $\widehat{\sigma}$  a scalar value that we assume constant for each component of the vector  $\mathbf{p}$ . The idea of the Metropolis-Hastings algorithm is to construct a posterior distribution of the parameter  $\pi_{\text{post}}(\mathbf{p})$  starting from some suitable assumptions on the prior distributions  $\pi_{\text{pr}}(\mathbf{p})$  of the parameters. In particular, in this work, we assume a uniform prior distribution of the parameters, with bounds  $a_\ell$  and  $b_\ell$  for the  $\ell$ -th component of the parameters vector  $\mathbf{p}$ .

At each iteration, we either accept or reject the new value of the chain, according to a Bernoulli distribution of parameter  $\rho$ , computed using the application of Bayes' theorem and defined by:

$$\rho = \frac{\pi_{\text{post}}(\mathbf{p}^* | \mathcal{Q}^{\text{PET}})}{\pi_{\text{post}}(\mathbf{p}^{(i-1)} | \mathcal{Q}^{\text{PET}})} = \frac{\pi(\mathcal{Q}^{\text{PET}} | \mathbf{p}^*)}{\pi(\mathcal{Q}^{\text{PET}} | \mathbf{p}^{(i)})} \cdot \frac{\pi_{\text{pr}}(\mathbf{p}^*)}{\pi_{\text{pr}}(\mathbf{p}^{(i)})}, \quad (8)$$

where  $\pi(\mathcal{Q} | \mathbf{p})$  is the conditioned distribution of the quantity of interest, with respect to the parameters' realization. The computation of this quantity requires that we assume a model for the uncertainty in the measuring errors. In particular, we can assume that the errors are distributed as a vectorial Gaussian distribution  $\mathcal{N}(\mathbf{0}, \sigma^2 \mathbf{I})$ . In this way, we can obtain a formula for the likelihood distribution:

$$\mathcal{Q}^{\text{PET}} | \mathbf{p} = \mathcal{N}(\mathcal{Q}(\mathbf{p}), \sigma^2 \mathbf{I}). \quad (9)$$

The MCMC algorithm is reported in Algorithm 1. At the end of the iterations, we compute the vector of the mean  $\mu_\ell$  and variance  $\sigma_\ell^2$  of the realizations of the  $p_\ell$  parameter. However, we neglect the first  $\widetilde{M}$  realizations, to eliminate the dependency on the initial point of the chain. More on MCMC methods can be found in [22].

### 3.2. Forward Uncertainty Quantification

The FK equation (2) depends on the vector of parameters  $\mathbf{p} = (p_1, \dots, p_N) \in \Gamma$ , whose random distribution can be determined following the procedure presented in Section 3.1. In particular, as an output of the inverse UQ problem, we have the set of pairs  $\{(\mu_\ell, \sigma_\ell)\}_{\ell=1}^N$ , where each  $(\mu_\ell, \sigma_\ell)$  denotes the mean and standard deviation of the normal-distributed parameter  $p_\ell \sim \mathcal{N}(\mu_\ell, \sigma_\ell)$ . Note that each  $p_\ell$  takes values in the entire real axes, namely,  $\Gamma_\ell = \mathbb{R}$ , whence  $\Gamma = \mathbb{R}^N$ . Moreover, we denote with  $\rho: \Gamma \rightarrow \mathbb{R}_+$  the joint probability density function (pdf) of  $\mathbf{p}$ . If the entries of  $\mathbf{p}$  are independent, then  $\rho = \prod_{\ell=1}^N \rho_\ell$ , where  $\rho_\ell: \Gamma_\ell \rightarrow \mathbb{R}_+$  denotes the pdf of a Gaussian random variable  $\rho_\ell(y) = \frac{1}{\sqrt{2\pi}\sigma_\ell} \exp\left(-\frac{y-\mu_\ell}{2\sigma_\ell^2}\right)$ .

In this framework, we are interested in quantifying how the uncertainty in the input parameter vector  $\mathbf{p}$  affects the QoI, by computing its statistical moments, like expectation and variance, respectively given by

$$\begin{aligned} \mathbb{E}[\mathcal{Q}] &= \int_{\Gamma} \mathcal{Q}(\mathbf{p}) \rho(\mathbf{p}) d\mathbf{p}, \\ \mathbb{V}[\mathcal{Q}] &= \int_{\Gamma} (\mathcal{Q}(\mathbf{p}) - \mathbb{E}[\mathcal{Q}(\mathbf{p})])^2 \rho(\mathbf{p}) d\mathbf{p}. \end{aligned} \quad (10)$$

In particular, in our medical application, we aim at quantifying the impact of varying piecewise constant reaction coefficients of prionic proteins on the onset and progression of Alzheimer's disease.

#### 3.2.1. MC method

The easiest and most popular approach to compute approximations to the statistical moments defined in equation (10) is the MC method. The MC algorithm (in its plain formulation) computes the estimators for the

---

**Algorithm 1** MCMC estimation of the distribution of  $\mathbf{p}$

---

**Require:** Initial value of input parameter  $\mathbf{p}^{(0)}$

**Ensure:** Samples of the distribution  $\mathbf{p}^{(1:M)}$

**for**  $i = 1 : M$  **do**

    Extract the white noise value  $\boldsymbol{\delta}^* \sim \mathcal{N}(\mathbf{0}, \Sigma_p)$

    Compute  $\mathbf{p}^* = \mathbf{p}^{(i-1)} + \boldsymbol{\delta}^*$

    Compute  $c^* = c^*(\mathbf{x}, t, \mathbf{p}^*)$  by solving equation (6)

    Evaluate the QoI  $\mathcal{Q}^*$  at  $c^*$

    Compute the acceptance rate  $\rho = \frac{\pi_{\text{post}}(\mathbf{p}^* | \mathcal{Q}^{\text{PET}})}{\pi_{\text{post}}(\mathbf{p}^{(i-1)} | \mathcal{Q}^{\text{PET}})}$

    Extract from the Bernoulli the choice of accepting or not  $y \sim Be(\rho)$

**if**  $y = 1$  **then**

$\mathbf{p}^{(i)} = \mathbf{p}^*$

**else**

$\mathbf{p}^{(i)} = \mathbf{p}^{(i-1)}$

**end if**

**end for**

Discard the first  $\widetilde{M}$  realization of the Markov chain

Compute the mean of the parameters' realizations:

$$\mu_\ell = \frac{1}{M - \widetilde{M}} \sum_{j=\widetilde{M}+1}^M p_\ell^{(j)}$$

Compute the variance of the parameters' realizations:

$$\sigma_\ell^2 = \frac{1}{M - \widetilde{M} - 1} \sum_{j=\widetilde{M}+1}^M \left( (p_\ell^{(j)})^2 - \mu_\ell^2 \right)$$


---

expectation and variance as follows:

$$\begin{aligned} \mathbb{E}[\mathcal{Q}] &\simeq \mu_Q = \frac{1}{Q} \sum_{q=1}^Q \mathcal{Q}(c^{(q)}), \\ \mathbb{V}[\mathcal{Q}] &\simeq \sigma_Q^2 = \frac{1}{Q-1} \sum_{q=1}^Q \left( \mathcal{Q}(c^{(q)}) - \mu_Q \right)^2, \end{aligned} \tag{11}$$

see also Algorithm 2. Standard analysis results show that the MC error is  $O(Q^{-1/2})$ , namely it decays as the number of samples  $Q$  increases, with rate  $-\frac{1}{2}$ .

### 3.2.2. Sparse grid SC method

A successful alternative approach to performing forward UQ is the SC method based on sparse grids. It can be informally described as an approximation technique, obtained as a linear combination of several tensor product interpolation operators  $\Gamma$ , each formed by a limited number of points. The underlying idea is the so-called *sparsification principle*: while none of these tensor product interpolation operators will be very accurate, an overall good approximation can be recovered by carefully combining many of them. This comes at a much lower cost than that required by considering a full tensor product approach over the entire parameter space  $\Gamma$ . Indeed, such an approach would involve a number of grid points exponential in  $N$  hence it would be affected by the so-called curse of dimensionality. Consequently, the full tensor product approach is unfeasible, even for moderately small  $N$ .

---

**Algorithm 2** MC estimators for expectation and variance

---

**Require:**  $Q$

**Ensure:** MC estimators  $\mu_Q, \sigma_Q^2$

Set  $\mu_Q = 0, \nu_Q = 0$

Generate  $Q$  i.i.d. samples of the input parameter  $\mathbf{p}, \{\mathbf{p}^{(q)}\}_{q=1}^Q$

**for**  $q = 1 : Q$  **do**

    Compute  $c^{(q)} = c^{(q)}(\mathbf{x}, t, \mathbf{p}^{(q)})$  by solving equation (6)

    Evaluate the QoI at  $c^{(q)}$

$\mu_Q = \mu_Q + \mathcal{Q}(c^{(q)})$

$\nu_Q = \nu_Q + \mathcal{Q}(c^{(q)})^2$

**end for**

$\sigma_Q^2 = \frac{1}{Q-1} (\nu_Q - \mu_Q^2)$

$\mu_Q = \frac{1}{Q} \mu_Q$

---

*One-dimensional Stochastic Collocation*

The starting point for the construction of the sparse grid approximation to the QoI relies on the introduction of one-dimensional Lagrange interpolation operators  $\mathcal{U}^{m(i_n)}: C^0(\Gamma_n) \rightarrow P_{m(i_n)-1}(\Gamma_n)$  for all  $n = 1, \dots, N$ , given by

$$\mathcal{U}^{m(i_n)}[u](p_n) = \sum_{j_n=1}^{m(i_n)} u(p_n^{(j_n)}) \ell_j(p_n^{(j_n)}) \quad \forall p_n \in \Gamma_n, \tag{12}$$

where  $\mathcal{H}_{n,m(i_n)} = \{p_n^{(j_n)}\}_{j_n=1}^{m(i_n)}$  and  $\{\ell_{j_n}\}_{j_n=1}^{m(i_n)}$  denote the set of Lagrange abscissas (or collocation points) and Lagrange polynomials of degree  $m(i_n)$ , respectively. Here  $i_n \geq 1$  is an integer denoting the level of approximation and  $m(i_n)$  is the number of collocation points used to build the interpolation at level  $i_n$ . The choice of the collocation points depends on the distribution of the random parameter  $p_n$ . In the particular case where  $p_n$  follows a Gaussian distribution (as in the present paper), possible choices are Gauss-Hermite points, GenzKeister points or Leja points. As  $i_n$  varies, we get a sequence of Lagrange interpolation operators  $\{\mathcal{U}^{m(i_n)}\}_{i_n \geq 1}$ . As a function of  $i_n$ , the (level-to-knot) function  $m(i_n)$  has to fulfill:  $m(0) = 0$  (and  $\mathcal{U}^0 = 0$ ),  $m(1) = 1$  and  $m(i_n) < m(i_n + 1)$  for  $i_n \geq 1$ .

*Smolyak sparse grids*

Let  $\mathbf{i} = (i_1, \dots, i_N) \in \mathbb{N}_+^N$  be the multi-index with entries representing the approximation level along each direction  $n$ , for  $n = 1, \dots, N$ . Given the  $N$ -dimensional set of collocation points

$$\mathcal{H}_{m(\mathbf{i})} = \prod_{n=1}^N \mathcal{H}_{n,m(i_n)}$$

being the Cartesian product of the one-dimensional sets of collocation points  $\mathcal{H}_{1,m(i_1)}, \dots, \mathcal{H}_{N,m(i_N)}$ , we introduce the tensor product interpolation operator  $\mathcal{U}^{m(\mathbf{i})} = \mathcal{U}^{m(i_1)} \otimes \dots \otimes \mathcal{U}^{m(i_N)}$  given by

$$\mathcal{U}^{m(\mathbf{i})}[u](\mathbf{p}) = \sum_{j_1=1}^{m(i_1)} \dots \sum_{j_N=1}^{m(i_N)} u(p_1^{(j_1)}, \dots, p_N^{(j_N)}) (\ell_{j_1} \otimes \dots \otimes \ell_{j_N})(\mathbf{p}) \tag{13}$$

for all  $u \in C^0(\Gamma)$ . Note that the set  $\mathcal{H}_{m(\mathbf{i})}$  contains  $\#\mathcal{H}_{m(\mathbf{i})} = \prod_{n=1}^N m(i_n)$  collocation points. Hence, the tensor product interpolation operator  $\mathcal{U}^{m(\mathbf{i})}$  requires  $\#\mathcal{H}_{m(\mathbf{i})}$  evaluations of  $u$ . For example, when taking  $u = \mathcal{Q}$  as in equation (7) being the spatial average of the FK solution at final time  $T$ , we get

$$\mathcal{Q}(\mathbf{p}) \sim \mathcal{U}^{m(\mathbf{i})}[\mathcal{Q}](\mathbf{p})$$



The Smolyak sparse grid approximation to the QoI  $\mathcal{Q}$  is the combination technique:

$$\mathcal{S}_I[\mathcal{Q}](\mathbf{p}) = \sum_{\mathbf{i} \in I} \gamma_{\mathbf{i}} \mathcal{U}^{m(\mathbf{i})}[\mathcal{Q}](\mathbf{p}), \tag{14}$$

where

- $\{\gamma_{\mathbf{i}}\}_{\mathbf{i} \in I}$  are the combination technique coefficients, given by  $\gamma_{\mathbf{i}} = \sum_{\substack{j \in \{0,1\}^N \\ \mathbf{i} + \mathbf{j} \in I}} (-1)^{|\mathbf{j}|}$ . Note that some  $c_{\mathbf{i}}$  might be null, in which case  $\mathcal{U}^{m(\mathbf{i})}$  does not enter in the final approximation;
- $I \subset \mathbb{N}_+^N$  is a set of multi-indices that specifies which tensor interpolation operators enter in the sparse grid construction. It should be chosen according to the sparsification principle, namely, whenever one entry of  $\mathbf{i}$  is large, the others should be kept as small as possible. Moreover, it is required to be downward-closed, namely, if  $\mathbf{i} \in I$ , then  $\mathbf{i} - \mathbf{e}_n \in I$ , for all  $n = 1, \dots, N$ , where  $\mathbf{e}_n$  denotes the vector with all zeros except the  $n$ -th component, that is equal to 1.

Note that equation (14) requires to solve equation (6) at all the collocation points  $\mathbf{p}$  in the sparse grid

$$\mathcal{H}_I = \bigcup_{\mathbf{i} \in I} \mathcal{H}_{m(\mathbf{i})}.$$

Moreover, it becomes operative as far as we specify the three basic “ingredients” of the sparse grid construction, namely, the set  $I$ , the level-to-knot function  $m(\cdot)$ , and the one-dimensional knots used along each direction  $n = 1, \dots, N$ . In Section 4 we will detail our choices.

*Sparse grids for forward UQ*

Associated with the Smolyak sparse grid approximant (14) we introduce the sparse grid quadrature formula

$$Q_I[\mathcal{Q}] = \sum_{\mathbf{i} \in I} c_{\mathbf{i}} Q_{\mathbf{i}}[\mathcal{Q}], \tag{15}$$

where  $Q_{\mathbf{i}}$  denotes the tensor product quadrature rule

$$\int_{\Gamma} \mathcal{Q}(\mathbf{p}) \rho(\mathbf{p}) d\mathbf{p} \approx Q_{\mathbf{i}}[\mathcal{Q}] := \sum_{j_1=1}^{m(i_1)} \cdots \sum_{j_N=1}^{m(i_N)} \mathcal{Q}(p_1^{(j_1)}, \dots, p_N^{(j_N)}) q_1^{(j_1)} \cdots q_N^{(j_N)}$$

and  $q_n^{(j_n)} = \int_{\Gamma_n} \ell_{j_n}(p_n) \rho_n(p_n) dp_n$  for all  $n = 1, \dots, N$ .

Applying (15), we obtain the sparse grid approximations of the expectation and variance of the QoI:

$$\mathbb{E}[\mathcal{Q}] \approx Q_I[\mathcal{Q}], \quad \mathbb{V}[\mathcal{Q}] \approx Q_I[\mathcal{Q}^2] - (Q_I[\mathcal{Q}])^2.$$

### 4. NUMERICAL RESULTS

The numerical results presented in this section concern a patient-specific test case. In particular, we are considering a patient affected by Alzheimer’s disease, with a calibration phase that goes from the age of 61 years to 68 years. Indeed, the computational domain is reconstructed from medical images (see Sect. 4.1), and the distribution of the reaction parameters in the different regions of the brain is recovered by solving an inverse UQ problem (see Sect. 4.2). As the last step of our numerical study, we perform a forward UQ analysis (see Sect. 4.3), with the aim of determining the evolution of the Amyloid- $\beta$  protein for the next twenty years, taking as initial condition the data provided from the corresponding PET image. We mention that all the medical images we use in this section are provided by the OASIS-3 database (a freely available neuroimaging data set of the brain) [19]. In particular, the specific brain geometry considered in this work is displayed in Figure 2a. The numerical solver used for space discretization is based on a built-in MATLAB code, whereas for the SC method we employ the Sparse Grids Matlab kit [21]. The time discretization step is set equal to  $\Delta t = 2 \times 10^{-1}$  years in all the simulations.

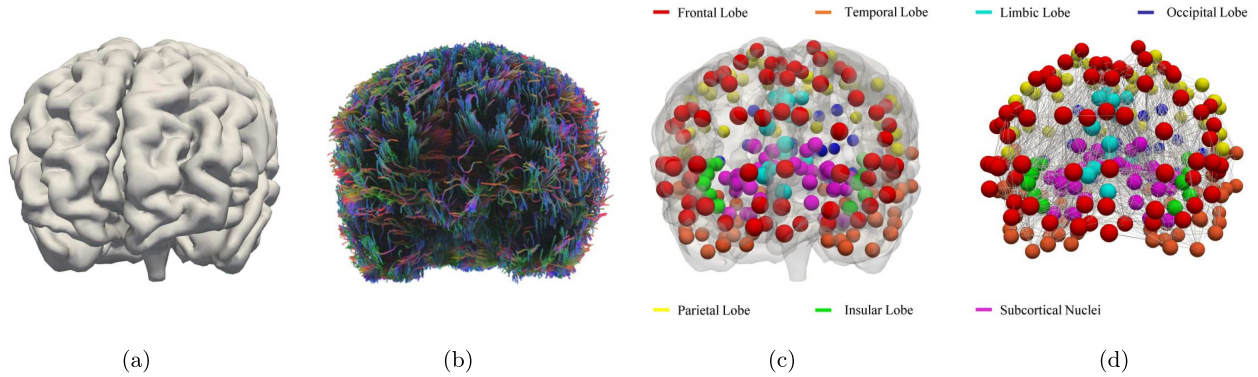


FIGURE 2. Graph discretization of the brain (each colour in Figures (c) and (d) denotes a different brain's region).

#### 4.1. Graph reconstruction and PET projection

To generate the graph modelling the brain network we employ DWI, a Magnetic Resonance Imaging (MRI) technique, which determines the Brownian motion of the water molecules; indeed the axonal nature of the neuronal connections creates directional paths for the motion. By using DSI studio [7], we can determine the brain's tractography, highlighting the axons' principal direction at every point of the brain [36], as we can observe in Figure 2b.

The tractography is used to derive a weighted graph  $\mathcal{G}$ , where the nodes in  $V$  are associated with a parcellation of the brain regions and the connecting edges  $E$  are weighted taking into account both the number of connections and the length of the paths. Starting from the tractography, the graph is reconstructed by counting the number of tracts  $n_{ij}$  that connect two brain regions associated with different nodes  $i$  and  $j$  and the mean value of the lengths of these tracts  $l_{ij}$ . Finally the weights  $w_{ij}$  of the graph are computed as follows:

$$w_{ij} = k \frac{n_{ij}}{l_{ij}} \quad i, j = 1, \dots, M, \quad (16)$$

where  $k$  is a scaling parameter adopted to reach a diffusivity value coherent to the literature values in similar works [9, 25]. In this work, we use parcellation based on the Brainnetome Atlas [8] and we group the nodes in 7 regions: frontal lobe, temporal lobe, parietal lobe, insular lobe, limbic lobe, occipital lobe, and subcortical nuclei. In Figure 2c we report the 246 nodes of the graph coloured according to the corresponding regions, and the edges of the graph are visible in Figure 2d. We report the local graphs of each region in Figure 3. Moreover, we display the connectogram representing the principal connections between different regions. For readability, the connectogram shows only the principal connections. More specifically, we show the ones associated with weights that are larger than a threshold, which we fix to be equal to the 5% of the maximum weight detected. We underline that the structure of the regions and the graph discretization have a large impact on the parameter calibration and then on the final output of the simulation, as it will be detailed in Section 4.2.

In order to estimate the reaction parameters as well as to set up the initial conditions for the (patient-specific) FK problem, we estimate the concentration  $c$  of Amyloid- $\beta$  protein at two different time instances. The medical data used are Positron Emission Tomography images with Pittsburgh compound B (PET-PiB) [33], which uses a radioligand able to identify the presence of Amyloid- $\beta$  plaques (more information on the acquisition techniques of the specific images used in this work can be found in [19]). The medical images are processed by means of the PET Unified Pipeline (PUP), to obtain a rescaling Standardized Uptake Value Ratio (SUVR). This scale is typically used in medical literature, to compare the images of different patients, and a value of the Amyloid positivity cutoff is estimated to be around 1.31 [19, 31]. The choice we make is to fit the value of positivity for

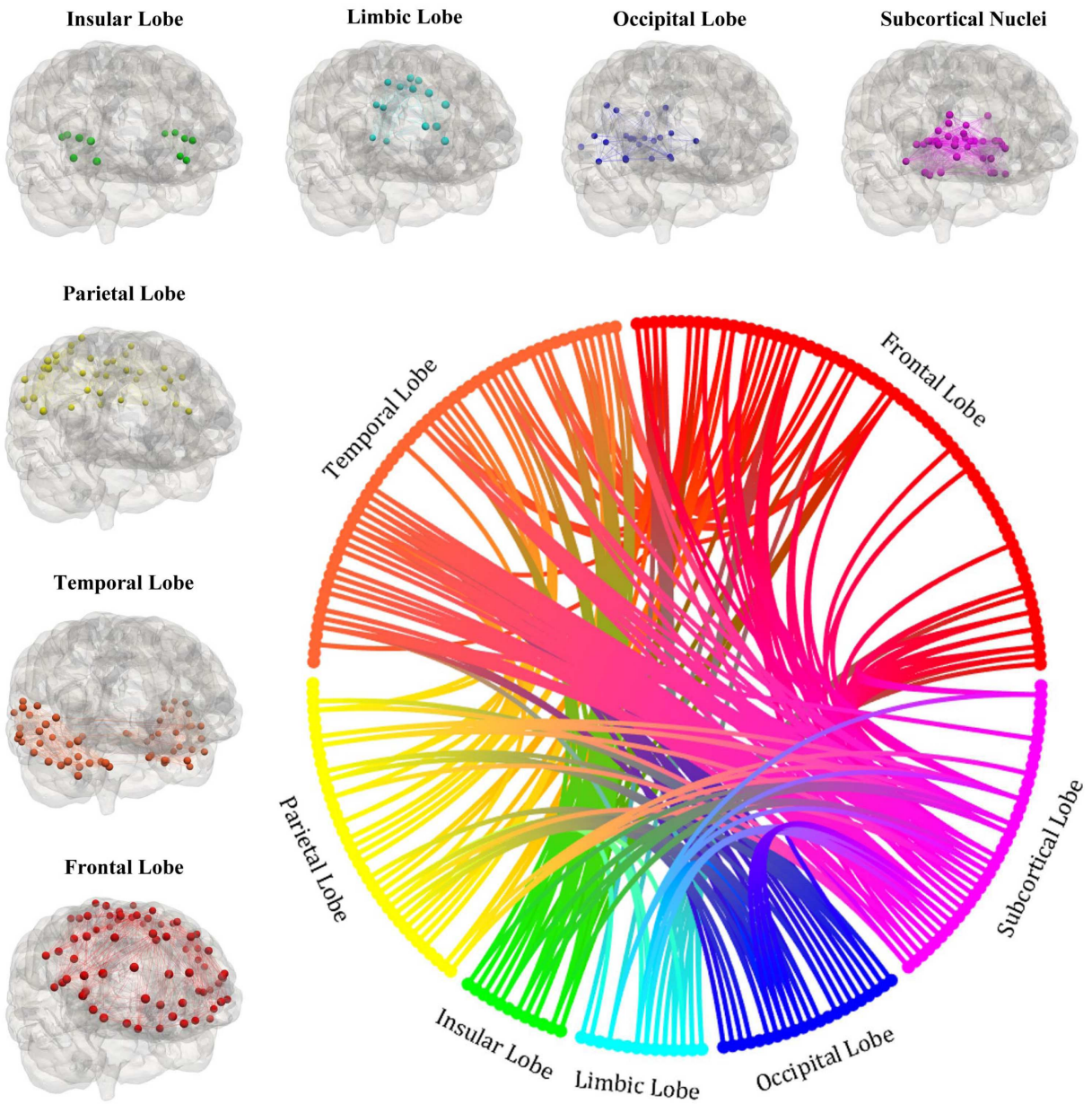


FIGURE 3. Local graphs of the seven regions of the brain and brain connectogram between different regions (excluding the connections with weight lower than 5% of the principal one).

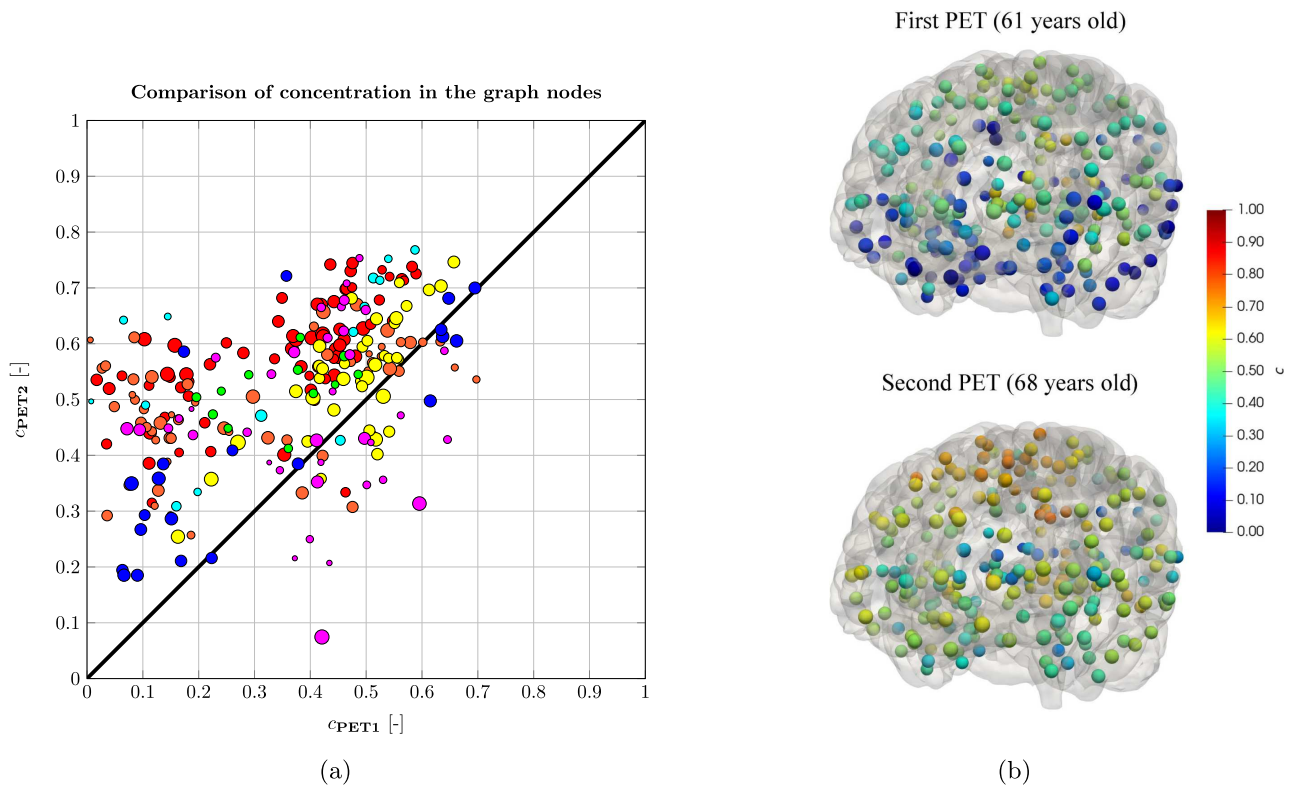


FIGURE 4. Data extracted from PET medical images. The first PET is acquired at 61 years, and the second one is acquired at 68 years. (a) Scatter plot of projected values from the PET in the nodes of the graph. The point color represents the region, the size is proportional to the volume of the node. (b) Projection of PET-PiB images on the reconstructed graph (first PET above and second one under). The color map refers to the level of proteins concentration.

the simulated concentration of FK equation to 0.75, and so make a rescale fixing  $c = 1$  as 1.74 of SUVR values in the PET image.

After having rescaled the values detected by the imaging so that they are between 0 and 1, we average the concentration on the parcellation reconstructed by DSI. Due to the fact that any region of the parcellation is associated with a single node in the brain connectome graph, we are obtaining the values of the concentration  $c_j$  at any node  $j$ . The output of the process is the projection of the medical images (at 61 and 68 years of the patient) on the reconstructed graph: see Figure 4b.

By comparing the two images in Figure 4b, we notice that the concentration of Amyloid- $\beta$  has increased in the majority of the graph nodes. A more precise comparison is provided in Figure 4a, where we plot the concentration of the second PET (at 68 years) versus that of the first (at 61 years). Each bullet is coloured according to the region it belongs to (the same color code as in Fig. 3 is employed) and its size is proportional to the volume of the represented brain section in the parcellation. The scatter plot confirms the increase of the concentration in most of the nodes. However, it seems that a few nodes exhibit a decrease in the concentration of misfolded proteins. This behaviour, which is mainly located in the subcortical lobe, is unexpected in the progress of the disease, that typically features an increase of the pathological proteins concentration. We attribute this inconsistency to the atrophy of the region, which can be observed in the MRI images around the ventricles, and which is typical of AD [33]. Indeed, a reduction of the tissue can affect the projection of the medical data on the

TABLE 1. Bounds of the prior uniform distributions of the parameters and mean and variance of the estimated distributions.

Brain Lobe (Index)	Parameter	Prior Distribution		Estimated Distribution	
		$a_\ell$	$b_\ell$	$\mu_\ell$	$\sigma_\ell^2$
Frontal Lobe (1)	$p_1$	-0.0700	0.4300	0.1801	0.0077
Temporal Lobe (2)	$p_2$	-0.1100	0.3900	0.1421	0.0079
Parietal Lobe (3)	$p_3$	-0.1900	0.3100	0.0627	0.0060
Insular Lobe (4)	$p_4$	-0.1500	0.3500	0.1005	0.0070
Limbic Lobe (5)	$p_5$	-0.1200	0.3800	0.1351	0.0075
Occipital Lobe (6)	$p_6$	-0.1900	0.3100	0.0545	0.0086
Subcortical Nuclei (7)	$p_7$	-0.1500	0.3500	0.1147	0.0093

graph, due to the fact that the same pixel of PET image catches a larger part of the domain without neuronal tissue.

### 4.2. Estimation of parameter distributions

In this section, we compute the distributions of the reaction parameters in the 7 regions of the graph by means of the inverse UQ process illustrated in Section 3.1. To better calibrate the distributions, we need to take into account the existence of some outliers in the PET measurements, as explained in Section 4.1. When calibrating the reaction parameters, we will not take into account those nodes at which the concentration in the second PET is lower than in the first one of more than 10%. This choice of cutoff is empirical and it is based on the literature evidence according to which, in general, the concentration of Amyloid- $\beta$  does not decrease over time [17, 29]. The choice of this cutoff at -10% preserves nodes in which we have a constant concentration of protein, but in which we register a small decrease due to some noise in the medical images.

According to (1), the reaction coefficient  $\alpha$  is modelled as a piecewise Gaussian random field, namely,  $\alpha$  is a Gaussian random variable whenever restricted to any of the seven brain regions. To model the reaction parameter as a Gaussian distribution is a typical choice in the literature of prionic proteins spreading [26, 27]. The complexity of the described underlying processes does not guarantee any bound on the values that the parameter can assume; in particular, it can be also negative (in case of high clearance in a specific region). However, the natural choice is a distribution with a positive mean value, as in [26]. Indeed, our choices are made to have a low probability of having negative values of the parameter. In particular, we optimize the average concentration of the protein in each region of the graph as follows:

$$Q_j = \langle c_h \rangle_j(T) = \sum_{k_j=1}^{M_j} c_{k_j}^{N_t} \frac{v_{k_j}}{v_{\text{tot}}} \quad j = 1, \dots, 7. \tag{17}$$

In equation (17) we are computing a weighted average on the  $j$ -th region of the graph (containing  $M_j$  nodes), for  $j = 1, \dots, 7$ . The concentration at each node  $c_{k_j}^{N_t}$  is weighted by the volume of the  $k_j$ -th node  $v_{k_j}$  and divided by the total volume  $v_{\text{tot}}$ . The corresponding index for each brain region is reported in Table 1.

The Metropolis-Hastings algorithm (see Algorithm 1) is initialized by using a step with standard deviation  $\hat{\sigma} = 10^{-2}$ . Moreover, we adopt a likelihood with standard deviation  $\sigma = 0.1$ . Finally, we choose the prior distribution for the 7 parameters as  $p_\ell \sim U(a_\ell, b_\ell)$ , where  $a_\ell$  and  $b_\ell$  are calibrated according to the available medical data (see Tab. 1). This mean value is also used to initialize the Markov chain, namely  $\mathbf{p}^{(0)} = \frac{1}{2}(\mathbf{a} + \mathbf{b})$ , where  $\mathbf{a} = (a_\ell)_\ell$  and  $\mathbf{b} = (b_\ell)_\ell$ . To neglect the impact of the initial choice, we eliminate from the mean and variance computation the first  $\tilde{M} = 10\,000$  steps out of the  $M = 100\,000$  we perform in this simulation.

The output values for  $\mu_\ell$  and  $\sigma_\ell^2$  are reported in Table 1. We can observe that the mean values feature high variability inside the different regions, and this result justifies the choice of using a non-homogeneous

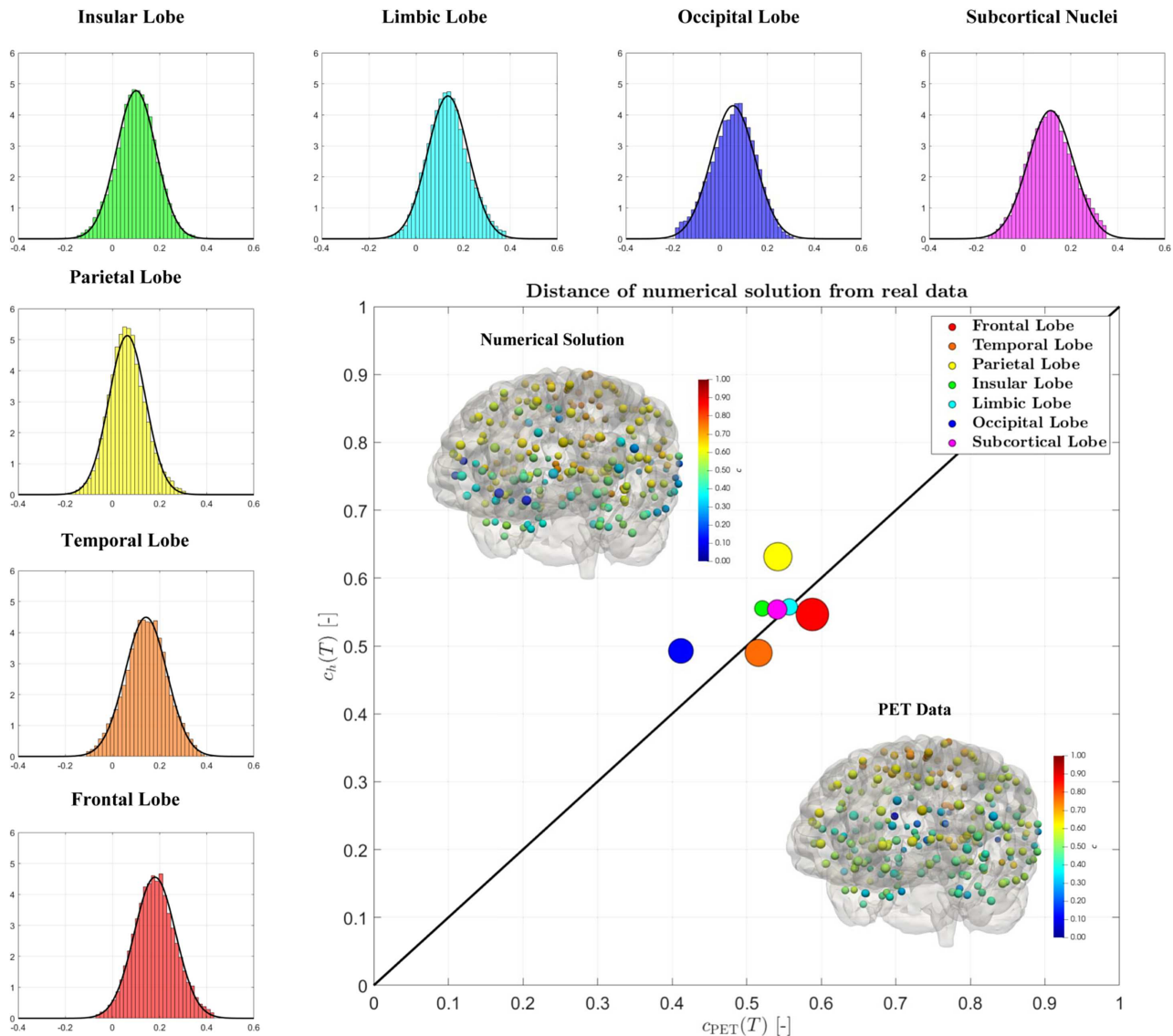


FIGURE 5. Results of the MCMC algorithm. Histogram and Gaussian distribution associated with each lobe of the brain and comparison between the medical data and the numerical results ( $T = 20$ ).

spatial description of the corresponding parameter. Moreover, in Figure 5 we display the 7 different estimated distributions with the histograms associated with the Markov chain realizations. We can observe coherence between the result of the MCMC algorithm and the resulting Gaussian probability distributions, that we use in the following section. Finally, in Figure 5 we report the comparison between the  $\mathcal{Q}$  computed starting from the numerical solution, obtained using the mean values of the parameters and the corresponding  $\mathcal{Q}$  derived from the medical images, neglecting the outliers as explained in Section 4.1. In the results reported in Figure 5 the size of the bullets is proportional to the volume of the lobes. The accuracy of the estimating algorithm for the parameters can be measured by the distance from the bisecting line, in which the numerical predicted value

would be exactly equal to the medical data from PET images. Finally, we report the numerical solution on the graph and the medical data at the final time. In both cases, we observe a higher concentration of misfolded proteins inside the parietal and frontal lobes, coherently to what we expect from the medical literature [15]. This shows that our numerical method is able to reproduce the disease progression.

### 4.3. Prediction of disease development

In this section, we simulate future scenarios of the development of the Amyloid- $\beta$  concentration inside the brain, by following the two approaches presented in Section 3.2, namely MC and SC.

In this simulation, we fix the final time at  $T = 20$  years and we discretize the time interval  $[0, T]$  with a timestep  $\Delta t = 0.02$  years (we denote the set of all considered time instances as  $\mathcal{I}_T$ ). As QoI we choose the spatial average of the concentration inside the seven lobes of the brain graph, evaluated at all time instances  $t \in \mathcal{I}_T$ . In particular, at every  $t \in \mathcal{I}_T$ , we have a vectorial QoI  $\mathcal{Q} = (\mathcal{Q}_1, \dots, \mathcal{Q}_7)$ , where the  $j$ -th component is  $\mathcal{Q}_j = \langle c_h \rangle_j(t)$  for  $j = 1, \dots, 7$ . We aim at approximating the expected value and the variance of each of the QoI.

The reference expectation and variance are computed using the SC method on a Smolyak sparse grid of level 9 with Leja points (in total, there are 224 143 collocation nodes). The reference expectation and variance are denoted by  $\boldsymbol{\mu}_Q$  and  $\boldsymbol{\sigma}_Q^2$ , respectively, and they are both vectors of length 7: their different components correspond to the regions of the brain graph. In Figure 6a, we report the computed results in terms of the volume-weighted mean value over the different lobes  $\langle \boldsymbol{\mu}_Q \rangle$  and a range of standard deviation  $[\langle \boldsymbol{\mu}_Q \rangle - \langle \boldsymbol{\sigma}_Q \rangle; \langle \boldsymbol{\mu}_Q \rangle + \langle \boldsymbol{\sigma}_Q \rangle]$ . We observe a global increase of prionic concentration in time, coherently to what expected by the disease progression [15]. Moreover, the stochastic description yields an increasing uncertainty over the years, which allows for obtaining a range of future possible scenarios after many years.

We carry out a convergence analysis, with the aim of assessing the approximation properties of Smolyak sparse grids with increasing level  $w = 3, 4, 5, 6, 7, 8$ . The errors are reported in Table 2. We can notice that both for  $\langle \boldsymbol{\mu}_Q \rangle$  and  $\langle \boldsymbol{\sigma}_Q^2 \rangle$ , we have a monotone decrease of the error as the number of collocation points increases. We can also notice, that the accuracy of the approximation deteriorates as time advances. Indeed, it is reasonable that it is necessary to use a larger number of points, to approximate phenomena with larger variance, such as the concentration after 15-20 years. The convergence results for the SC method are also displayed in Figures 6a and 6b, where the errors at time instances  $t = 5, 10, 15, 20$  are reported versus the number of collocation points. For the sake of comparison, we also report the convergence of the MC error versus the number of MC samples (note that the MC error decays with the predicted rate  $M^{-1/2}$ ,  $M$  being the number of samples). We notice that, with a comparable number of evaluations of the differential problem, the SC method provides a more accurate solution. This is particularly pronounced for smaller time instances.

In Table 3 we report the expectation and variance of the averaged concentration inside every single region at time instances  $t = 5, 10, 15, 20$ . As we can notice, the expectation is increasing in time within each lobe, coherently with what we expect from the progression of the pathology. However, we can also notice that the variance is increasing only for the initial times, and when the expectation becomes larger than 0.8 it starts decreasing due to the impossibility of the solution to overcome 1, for the structure of FK equation [23]. For example, concerning the frontal lobe, we can observe a reduction in the variance, associated with the high values of protein concentration. In Figure 7 each row corresponds to a different lobe of the brain. In the first column, we display the evolution of the average protein concentration with the relative standard deviation ranges; in the second column we report the error convergence for SC versus the number of collocation points; in the third column the report the MC error versus the number of samples. We notice that also considering the regional average concentrations the SC method allows for reaching a more precise solution than MC, with a comparable number of evaluations of the differential problem. However, in this case, the SC error does not decrease monotonically (this is likely due to the nonlinearity of the PDE). Finally, we notice that, compared with the global solution in Figure 6, we have a larger variability of the solution in the different regions, particularly after 20 years.

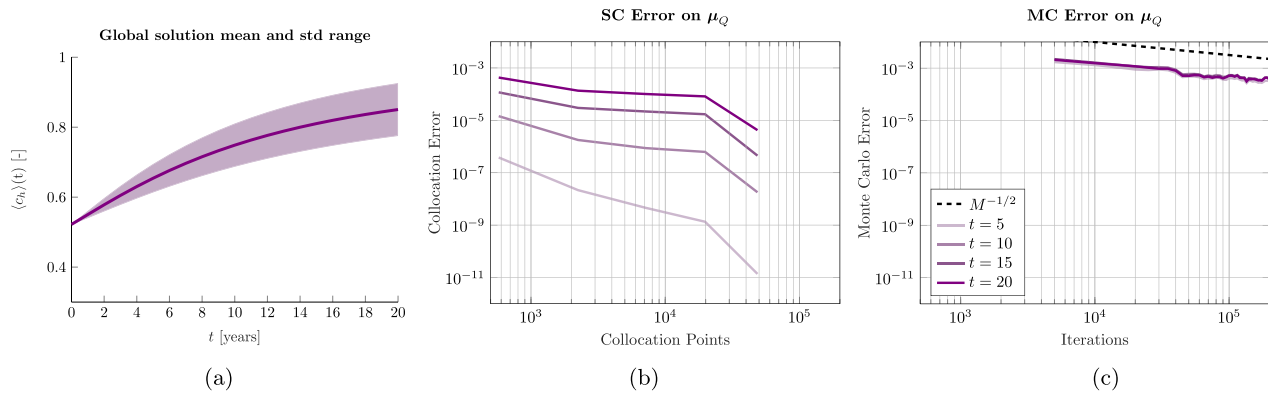


FIGURE 6. Numerical results of the SC and MC convergence tests for the average solution over the whole graph. (a) Result of the simulation in terms of average over the whole brain. (b) Stochastic collocation errors at different times snapshots. (c) MC errors versus  $M$  at different times snapshots, (convergence rate  $-1/2$ ).

TABLE 2. Bounds of the prior uniform distributions of the parameters and expectation and variance of the estimated distributions.

Grid level	3	4	5	6	7	8
Collocation Points	375	2241	7183	19825	48639	108545
Collocation errors on approximation of $\langle \mu_Q \rangle$						
Time: $t = 5$	$3.81 \times 10^{-7}$	$2.15 \times 10^{-8}$	$4.54 \times 10^{-9}$	$1.34 \times 10^{-9}$	$1.37 \times 10^{-11}$	$3.82 \times 10^{-12}$
Time: $t = 10$	$1.44 \times 10^{-5}$	$1.77 \times 10^{-6}$	$8.69 \times 10^{-7}$	$6.23 \times 10^{-7}$	$1.79 \times 10^{-8}$	$1.61 \times 10^{-8}$
Time: $t = 15$	$1.17 \times 10^{-4}$	$2.98 \times 10^{-5}$	$2.17 \times 10^{-5}$	$1.70 \times 10^{-5}$	$4.48 \times 10^{-7}$	$4.55 \times 10^{-7}$
Time: $t = 20$	$4.29 \times 10^{-4}$	$1.35 \times 10^{-4}$	$1.01 \times 10^{-4}$	$8.21 \times 10^{-5}$	$4.22 \times 10^{-6}$	$2.17 \times 10^{-6}$
Collocation errors on approximation of $\langle \sigma_Q^2 \rangle$						
Time: $t = 5$	$5.69 \times 10^{-5}$	$4.20 \times 10^{-6}$	$1.26 \times 10^{-6}$	$5.34 \times 10^{-7}$	$6.42 \times 10^{-9}$	$3.37 \times 10^{-9}$
Time: $t = 10$	$2.24 \times 10^{-3}$	$4.32 \times 10^{-4}$	$2.36 \times 10^{-4}$	$1.50 \times 10^{-4}$	$4.43 \times 10^{-6}$	$2.03 \times 10^{-6}$
Time: $t = 15$	$8.06 \times 10^{-3}$	$2.21 \times 10^{-3}$	$1.40 \times 10^{-3}$	$1.03 \times 10^{-3}$	$9.59 \times 10^{-5}$	$2.78 \times 10^{-5}$
Time: $t = 20$	$1.62 \times 10^{-2}$	$5.56 \times 10^{-3}$	$4.68 \times 10^{-3}$	$3.94 \times 10^{-3}$	$4.99 \times 10^{-4}$	$1.56 \times 10^{-4}$

TABLE 3. Expectation and variance of the solution distributions inside the brain regions.

Brain Lobe (Index)	$t = 5$		$t = 10$		$t = 15$		$t = 20$	
	$\mu_Q$	$\sigma_Q^2$	$\mu_Q$	$\sigma_Q^2$	$\mu_Q$	$\sigma_Q^2$	$\mu_Q$	$\sigma_Q^2$
Frontal Lobe (1)	0.7527	0.0049	0.8486	0.0078	0.9000	0.0077	0.9289	0.0069
Temporal Lobe (2)	0.6515	0.0063	0.7598	0.0117	0.8277	0.0128	0.8699	0.0122
Parietal Lobe (3)	0.6018	0.0060	0.6729	0.0156	0.7303	0.0226	0.7738	0.0265
Insular Lobe (4)	0.6417	0.0061	0.7405	0.0123	0.8096	0.0142	0.8558	0.0138
Limbic Lobe (5)	0.6914	0.0051	0.7892	0.0095	0.8514	0.0102	0.8905	0.0093
Occipital Lobe (6)	0.5121	0.0073	0.6043	0.0194	0.6782	0.0275	0.7336	0.0314
Subcortical Nuclei (7)	0.5822	0.0067	0.7066	0.0147	0.7891	0.0176	0.8413	0.0175



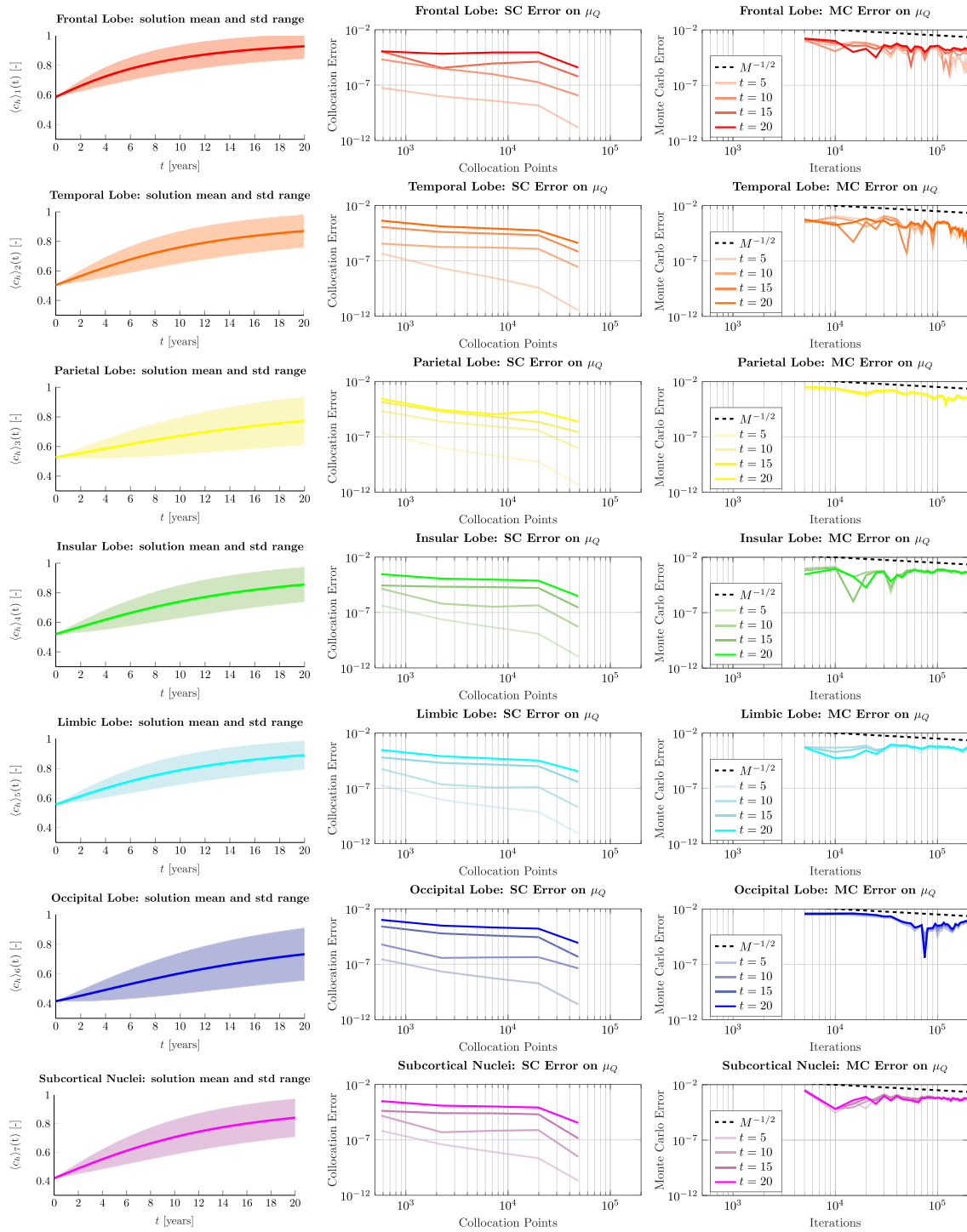


FIGURE 7. Numerical results of the simulation in terms of the average on every single lobe (on the left), collocation errors at different times (in the middle), MC errors versus  $M$  at different times snapshots  $t = 5, 10, 15, 20$  (on the right).

## 5. CONCLUSIONS

In this work, we have proposed an approach to predict the progression of the accumulation of misfolded Amyloid- $\beta$  proteins by means of a Fisher-Kolmogorov model in Alzheimers disease. In order to model the reaction coefficients, which cannot be measured and whose values depend on many different physical processes, we adopted a stochastic model. The evaluation of the distributions has been made by means of an inverse uncertainty quantification algorithm and then applied to the prediction of the disease development in the next 20 years.

To keep the computational cost affordable, a reduced-order model, based on a graph discretization of the brain connectome, is used. The derivation of the graph from medical images and the calibration of the parameter distributions by means of clinical data yielded a complete patient-specific model for the simulation of the progression of Alzheimer's disease. In the numerical results, we presented a comparison in applying the Monte Carlo algorithm with respect to a stochastic collocation, for estimating proteins' concentration. The tests confirm that the application of collocation on sparse grids yields a more precise approximation of the final solution, in particular for smaller time frames (5–10 years), with the same number of evaluations of the PDE solution.

Some future developments of this work could concern the extension of the uncertainty quantification analysis to the three-dimensional models, for example, applying the study to discontinuous Galerkin methods on real brain geometries. Another possible development is using a white noise description for the weights of the graphs that are computed starting from medical images and could be affected by measuring errors. In this context, a sensitivity analysis between the relative importance of diffusion and reaction in network modelling can be an interesting future development. Moreover, complete validation of the diffusion values by computing the values from medical images [32] is not performed in this work, but it could improve the procedure. Finally, it can be interesting to perform a complete analysis on a large number of different patients, to highlight the differences in the computed values among them.

*Acknowledgements.* The brain MRI images were provided by OASIS-3: Longitudinal Multimodal Neuroimaging: Principal Investigators: T. Benzinger, D. Marcus, J. Morris; NIH P30 AG066444, P50 AG00561, P30 NS09857781, P01 AG026276, P01 AG003991, R01 AG043434, UL1 TR000448, R01 EB009352.

*Declaration of competing interests.* The authors declare that they have no known competing financial interests or personal relationships that could have appeared to influence the work reported in this article.

*Funding.* PFA has been partially funded by the research grants PRIN2017 n. 201744KLJL funded by MUR. PFA and AMQ have been partially funded by the research grants PRIN2020 n. 20204LN5N5 funded by MUR. PFA has been partially supported by ICSC–Centro Nazionale di Ricerca in High Performance Computing, Big Data, and Quantum Computing funded by European Union–NextGeneration EU. FB is partially funded by “INdAM - GNCS Project”, codice CUP E53C22001930001. The present research has been supported by MUR, grant Dipartimento di Eccellenza 2023-2027. MC, FB, PFA and AMQ are members of INdAM-GNCS.

## REFERENCES

- [1] I. Babuška, F. Nobile and R. Tempone, A stochastic collocation method for elliptic partial differential equations with random input data. *SIAM J. Numer. Anal.* **45** (2007) 1005–1034.
- [2] R.F. Betzel and D.S. Bassett, Generative models for network neuroscience: Prospects and promise. *J. R. Soc. Interface* **14** (2017) 20170623.
- [3] G.S. Bloom, Amyloid- $\beta$  and tau: the trigger and bullet in Alzheimer disease pathogenesis. *JAMA Neurol.* **71** (2014) 505–508.
- [4] T. Bohr, P.G. Hjorth, S.C. Holst, S. Hrabtsov, V. Kiviniemi, T. Lilius, I. Lundgaard, K.-A. Mardal, E.A. Martens, Y. Mori, U.V. Ngerl, C. Nicholson, A. Tannenbaum, J.H. Thomas, J. Tithof, H. Benveniste, J.J. Iliff, D.H. Kelley and M. Nedergaard, The glymphatic system: Current understanding and modeling. *iScience* **25** (2022) 104987.
- [5] F. Bonizzoni, M. Braukhoff, A. Jngel and I. Perugia, A structure-preserving discontinuous Galerkin scheme for the Fisher–KPP equation. *Numer. Math.* **146** (2020) 119–157.
- [6] M. Corti, F. Bonizzoni, L. Dede', A.M. Quarteroni and P.F. Antonietti, Discontinuous Galerkin methods for Fisher-Kolmogorov equation with application to  $\alpha$ -synuclein spreading in Parkinson's disease. *Comput. Methods Appl. Mech. Eng.* **417** (2023) 116450.
- [7] DSI-Studio, A Tractography Software Tool for Diffusion MRI Analysis. <https://dsi-studio.labsolver.org/>.

- [8] L. Fan, H. Li, J. Zhuo, Y. Zhang, J. Wang, L. Chen, Z. Yang, C. Chu, S. Xie, A.R. Laird, P.T. Fox, S.B. Eickhoff, C. Yu and T. Jiang, The human Brainnetome Atlas: A new brain Atlas based on connectonal architecture. *Cereb. Cortex* **26** (2016) 3508–3526.
- [9] S. Fornari, A. Schäfer, M. Jucker, A. Goriely and E. Kuhl, Prion-like spreading of Alzheimer’s disease within the brain’s connectome. *J. R. Soc. Interface* **16** (2019) 20190356.
- [10] B. Franchi and S. Lorenzani, From a microscopic to a macroscopic model for Alzheimer disease: Two-scale homogenization of the Smoluchowski equation in perforated domains. *J. Nonlinear Sci.* **26** (2016) 717–753.
- [11] C. Godsil and G. Royle, Algebraic Graph Theory, 1st edition. Springer (2001).
- [12] A. Goriely, E. Kuhl and C. Bick, Neuronal oscillations on evolving networks: Dynamics, damage, degradation, decline, dementia, and death. *Phys. Rev. Lett.* **125** (2020) 128102.
- [13] J.H. Halton, A retrospective and prospective survey of the Monte Carlo method. *SIAM Rev.* **12** (1970) 1–63.
- [14] H. Hampel, K. Bürger, S.J. Teipel, A.L.W. Bokke, H. Zetterberg and K. Blennow, Core candidate neurochemical and imaging biomarkers of Alzheimer’s disease. *Alzheimer’s Dementia J. Alzheimer’s Assoc.* **4** (2008) 38–48.
- [15] H. Hampel, J. Hardy, K. Blennow, C. Chen, G. Perry, S.H. Kim, V.L. Villemagne, P. Aisen, M. Vendruscolo, T. Iwatsubo, C.L. Masters, M. Cho, L. Lannfelt, J.L. Cummings and A. Vergallo, The Amyloid- $\beta$  pathway in Alzheimer’s disease. *Mol. Psychiatry* **26** (2021) 5481–5503.
- [16] W.K. Hastings, Monte Carlo sampling methods using Markov Chains and their applications. *Biometrika* **57** (1970) 97–109.
- [17] C.R. Jack, H.J. Wiste, T.G. Lesnick, S.D. Weigand, D.S. Knopman, P. Vemuri, V.S. Pankratz, M.L. Senjem, J.L. Gunter, M.M. Mielke, V.J. Lowe, B.F. Boeve and R.C. Petersen, Brain  $\beta$ -amyloid load approaches a plateau. *Neurology* **80** (2013) 890–896.
- [18] D. Kaliuzhnyi-Verbovetskyi and G.S. Medvedev, The semilinear heat equation on sparse random graphs. *SIAM J. Math. Anal.* **49** (2017) 1333–1355.
- [19] P.J. LaMontagne, T.L. Benzinger, J.C. Morris, S. Keefe, R. Hornbeck, C. Xiong, E. Grant, J. Hassenstab, K. Moulder, A.G. Vlassenko, M.E. Raichle, C. Cruchaga and D. Marcus, Oasis-3: Longitudinal neuroimaging, clinical, and cognitive dataset for normal aging and alzheimer disease. *medRxiv* (2019).
- [20] F. Nobile, R. Tempone and C.G. Webster, A sparse grid stochastic collocation method for partial differential equations with random input data. *SIAM J. Numer. Anal.* **46** (2008) 2309–2345.
- [21] C. Piazzola and L. Tamellini, The Sparse Grids Matlab kit – a Matlab implementation of sparse grids for high-dimensional function approximation and uncertainty quantification. Preprint: [arXiv:2203.09314](https://arxiv.org/abs/2203.09314) (2022).
- [22] C.P. Robert and G. Casella, Monte Carlo Statistical Methods, 2nd edition. Springer (1999).
- [23] S. Salsa, Partial Differential Equations in Action: from Modeling to Theory, 3rd edition. Springer (2016).
- [24] A. Schäfer, J. Weickenmeier and E. Kuhl, The interplay of biochemical and biomechanical degeneration in Alzheimer’s disease. *Comput. Methods Appl. Mech. Eng.* **352** (2019) 369–388.
- [25] A. Schäfer, E.C. Mormino and E. Kuhl, Network diffusion modeling explains longitudinal tau PET data. *Front. Neurosci.* **14** (2020) 566876.
- [26] A. Schäfer, M. Peirlinck, K. Linka, E. Kuhl and ADNI, Bayesian physics-based modeling of Tau propagation in Alzheimer’s disease. *Front. Physiol.* **12** (2021) 1081.
- [27] A. Schäfer, P. Chaggar, A. Goriely, E. Kuhl and ADNI, Correlating tau pathology to brain atrophy using a physics-based Bayesian model. *Eng. Comput.* **38** (2022) 3867–3877.
- [28] P. Scheltens, B. De Strooper, M. Kivipelto, H. Holstege, G. Chtelat, C.E. Teunissen, J. Cummings and W.M. van der Flier, Alzheimer’s disease. *The Lancet* **397** (2021) 1577–1590.
- [29] C.G. Schwarz, M.L. Senjem, J.L. Gunter, N. Tosakulwong, S.D. Weigand, B.J. Kemp, A.J. Sychalla, P. Vemuri, R.C. Petersen, V.J. Lowe and C.R. Jack, Optimizing PiB-PET SUVR change-over-time measurement by a large-scale analysis of longitudinal reliability, plausibility, separability, and correlation with MMSE. *Neuroimage* **144** (2017) 113–127.
- [30] A.J. Smola and R. Kondor, Kernels and Regularization on Graphs, in *Learning Theory and Kernel Machines*. Springer (2003) 144–158.
- [31] Y. Su, S. Flores, G. Wang, R.C. Hornbeck, B. Speidel, N. Joseph-Mathurin, A.G. Vlassenko, B.A. Gordon, R.A. Koeppe, W.E. Klunk, C.R. Jack Jr., M.R. Farlow, S. Salloway, B.J. Snider, S.B. Berman, E.D. Roberson, J. Brosch, I. Jimenez-Velazques, C.H. van Dyck, D. Galasko, S.H. Yuan, S. Jayadev, L.S. Honig, S. Gauthier, G.-Y.R. Hsiung, M. Masellis, W.S. Brooks, M. Fulham, R. Clarnette, C.L. Masters, D. Wallon, D. Hannequin, B. Dubois, J. Pariente, R. Sanchez-Valle, C. Mummery, J.M. Ringman, M. Bottlaender, G. Klein, S. Milosavljevic-Ristic, E. McDade, C. Xiong, J.C. Morris, R.J. Bateman and T.L. Benzinger, Comparison of Pittsburgh compound B and florbetapir in cross-sectional and longitudinal studies. *Alzheimer’s Dement. Diagn. Assess. Dis. Monit.* **11** (2019) 180–190.
- [32] L.M. Valnes, S.K. Mitusch, G. Ringstad, P.K. Eide, S.W. Funke and K.-A. Mardal, Apparent diffusion coefficient estimates based on 24 hours tracer movement support glymphatic transport in human cerebral cortex. *Sci. Rep.* **10** (2020) 9176.
- [33] W.M. van Oostveen and E.C.M. de Lange, Imaging techniques in Alzheimer’s disease: A review of applications in early diagnosis and longitudinal monitoring. *Int. J. Mol. Sci.* **22** (2021) 2110.
- [34] L.C. Walker and M. Jucker, Neurodegenerative diseases: Expanding the prion concept. *Annu. Rev. Neurosci.* **38** (2015) 87–103.
- [35] J. Weickenmeier, M. Jucker, A. Goriely and E. Kuhl, A physics-based model explains the prion-like features of neurodegeneration in Alzheimer’s disease, Parkinson’s disease, and amyotrophic lateral sclerosis. *J. Mech. Phys. Solids* **124** (2019) 264–281.

[36] F.-C. Yeh, Shape analysis of the human association pathways. *Neuroimage* **223** (2020) 117329.



**Please help to maintain this journal in open access!**

This journal is currently published in open access under the Subscribe to Open model (S2O). We are thankful to our subscribers and supporters for making it possible to publish this journal in open access in the current year, free of charge for authors and readers.

Check with your library that it subscribes to the journal, or consider making a personal donation to the S2O programme by contacting [subscribers@edpsciences.org](mailto:subscribers@edpsciences.org).

More information, including a list of supporters and financial transparency reports, is available at <https://edpsciences.org/en/subscribe-to-open-s2o>.